

# Light activation of Orange Carotenoid Protein reveals bicycle-pedal single-bond isomerization

Received: 7 April 2022

Accepted: 14 October 2022

Published online: 28 October 2022

 Check for updates

Volha U. Chukhutsina<sup>1</sup>, James M. Baxter<sup>1</sup>, Alisia Fadini<sup>1</sup>, Rhodri M. Morgan<sup>1</sup>, Matthew A. Pope<sup>1</sup>, Karim Maghlaoui<sup>1</sup>, Christian M. Orr<sup>2</sup>, Armin Wagner<sup>2</sup> & Jasper J. van Thor<sup>1</sup>✉

Orange Carotenoid protein (OCP) is the only known photoreceptor which uses carotenoid for its activation. It is found exclusively in cyanobacteria, where it functions to control light-harvesting of the photosynthetic machinery. However, the photochemical reactions and structural dynamics of this unique photosensing process are not yet resolved. We present time-resolved crystal structures at second-to-minute delays under bright illumination, capturing the early photoproduct and structures of the subsequent reaction intermediates. The first stable photoproduct shows concerted isomerization of C9'-C8' and C7'-C6' single bonds in the bicycle-pedal (s-BP) manner and structural changes in the N-terminal domain with minute timescale kinetics. These are followed by a thermally-driven recovery of the s-BP isomer to the dark state carotenoid configuration. Structural changes propagate to the C-terminal domain, resulting, at later time, in the H-bond rupture of the carotenoid keto group with protein residues. Solution FTIR and UV/Vis spectroscopy support the single bond isomerization of the carotenoid in the s-BP manner and subsequent thermal structural reactions as the basis of OCP photoreception.

Carotenoids are found in plants, algae, and microorganisms and constitute the most widely spread group of pigments<sup>1</sup>. Carotenoids are isoprenoids which consist of a central carbon chain of alternating single and double bonds with unique photochemical properties. The S0-S1 electronic transition is optically forbidden in carotenoids and light absorption occurs through the intense S0-S2 transition<sup>2</sup> which is responsible for their yellow, orange and red colours. After light absorption, the S1 dark state is populated through internal conversion, which then relaxes with a picosecond lifetime<sup>3</sup>. The structure and conformation of carotenoids determine the energy landscape of their electronic states and, as a result, their biological functions. Carotenoid chromophores function as key photosynthetic regulators of biomass production<sup>4,5</sup> when their S1 states act as efficient quenchers of chlorophyll excited states<sup>6,7</sup>. Furthermore, carotenoid excited states also act as energy donors in

photosynthetic light-harvesting<sup>3</sup> as well as photoreceptors in light-signalling<sup>8</sup>. The structural and molecular basis for the diverse biological functions of carotenoid chromophores is of high importance and is necessary to fully understand in order to gain control of these processes. The carotenoid canthaxanthin (CAN) bound to the Orange Carotenoid Protein<sup>9,10</sup> is responsible for a light signalling function. OCP undergoes a photocycle<sup>9</sup> in which the keto-carotenoid also plays several different roles: in the inactive or orange state (OCP<sup>0</sup>, Fig. 1a), it senses blue-green light to initiate its photocycle, resulting in a final product that has undergone substantial structural conformational changes and exhibits distinct separation of the two OCP domains, namely, the all-helical N-terminal domain (NTD) and an  $\alpha/\beta$ -fold C-terminal domain (CTD)<sup>11</sup>. In the active state, following OCP<sup>R</sup> (red state) binding to the cyanobacterial light-harvesting antenna, the keto-carotenoid dissipates excess

<sup>1</sup>Department of Life Sciences, Imperial College London, London SW7 2AZ, UK. <sup>2</sup>Diamond Light Source, Harwell Science and Innovation Campus, Didcot OX11 0DE, UK. ✉e-mail: [j.vanthor@imperial.ac.uk](mailto:j.vanthor@imperial.ac.uk)

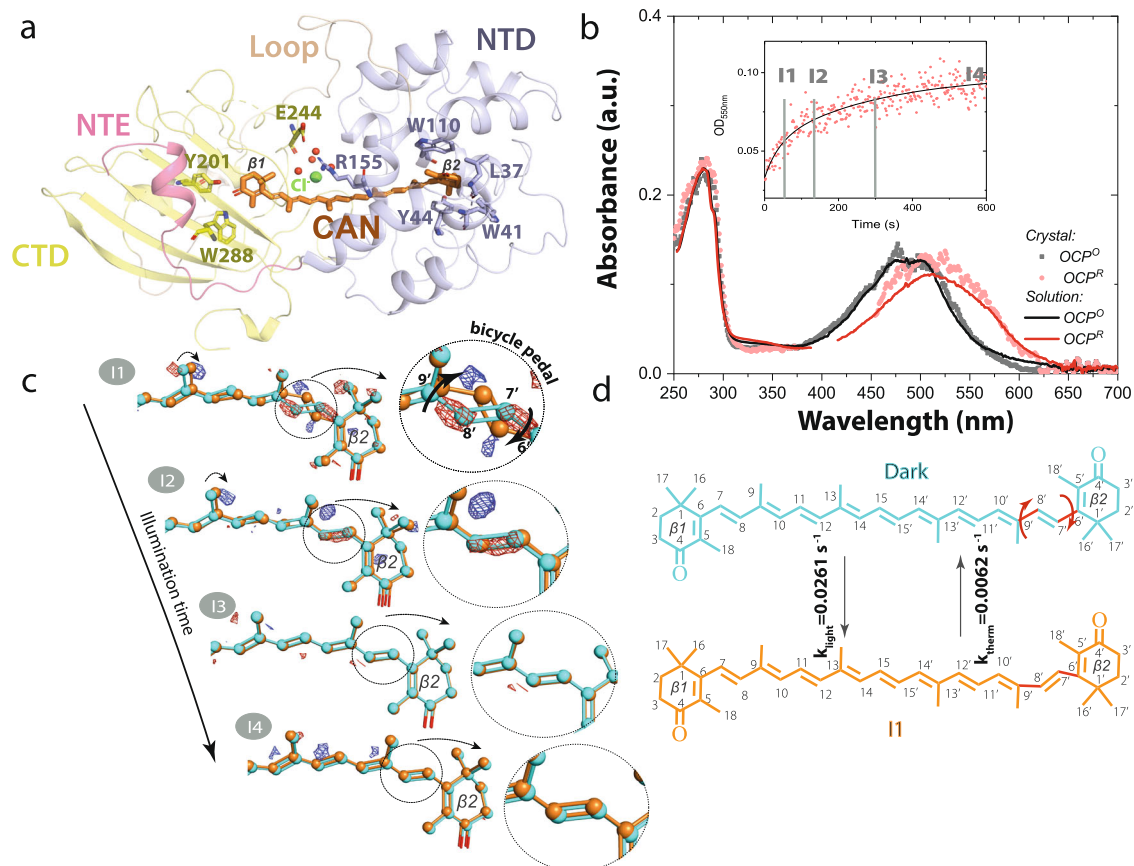


**Fig. 1 | Canthaxanthin single bond isomerization in the bicycle-pedal manner triggers OCP light activation.** **a** Structure of OCP in its inactive state ( $OCP^0$ ) displaying the C-terminal domain (CTD, yellow colour), N-terminal domain (NTD, violet colour), N-terminal extension (NTE, pink colour), and loop (wheat colour). The canthaxanthin (CAN) carotenoid is embedded between the two domains.  $Cl^-$  (in green) is resolved in the CTD where it coordinates four water molecules (in red) through ion-dipole interactions at distances of 3.0–4.0 Å. **b** Absorbance changes of OCP in solution (solid lines) and crystalline state (dotted lines) upon illumination with violet light (at 410 nm with 3.5 mWcm<sup>-2</sup> power; FWHM 20 nm of the emission spectrum). Inactive state  $OCP^0$  and active state  $OCP^R$  are shown in black/grey and red/pink respectively. The OD intensities are unavoidably polluted by the LED emission in 380–430 nm and therefore were omitted from the graph. Insert: Absorbance changes (pink dots) in the crystalline state detected at 550 nm upon 10 min of illumination. Black line represents double exponential fit of the curve

( $Y = A_1 e^{-t/\tau_1} + A_2 e^{-t/\tau_2}$ , where  $A_1 = 0.02$ ,  $\tau_1 = 38$  s and  $A_2 = 0.44$ ,  $\tau_2 = 291$  s). Grey labels indicate time points when I1–I4 intermediates have been cryotrapped. Source data are provided as a Source Data file. **c** Difference electron density (DED) maps were obtained for the four states: (I1) 1 min ( $F_{I1} - F_{Dark}$ ), (I2) 2 min ( $F_{I2} - F_{Dark}$ ), (I3) 5 min ( $F_{I3} - F_{Dark}$ ), (I4) 10 min ( $F_{I4} - F_{Dark}$ ). Red: negative DED, blue: positive DED on the  $-3\sigma/3\sigma$  contour levels, respectively. Carotenoid coordinates of dark ( $OCP^0$ ) and light states (I1–I4) are represented by cyan and orange lines respectively. Illuminated coordinates were obtained from extrapolated electron densities. Populations of the illuminated states obtained from the occupancy refinement (see “Methods”) are 15% (I1), 22% (I2), 25% (I3), and 32% (I4). Arrow in the insert in I1 state indicates carotenoid movement during illumination. **d** CAN in C9'-C8' *trans*/ C7'-C6' *cis* state is present in  $OCP^0$  while C9'-C8' *cis*/ C7'-C6' *trans* conformation (bicycle pedal isomerization) is observed in I1. The latter thermally recovers back to  $OCP^0$  CAN state with prolonged illumination time (after 2–5 min).

absorbed light energy through non-photochemical quenching (NPQ), a vital process for cyanobacterial survival in turbulent waters<sup>10,12</sup>. In cyanobacteria NPQ fully builds-up over minutes upon OCP control<sup>12,13</sup>. Therefore, resolving OCP photocycle is essential for understanding and controlling OCP photoregulation.

The mechanism and primary photochemical reaction of the keto-carotenoid that triggers this  $OCP^0$ - $OCP^R$  conversion is currently debated and requires structural evidence<sup>8,14</sup>. It has been argued that OCP photoactivation is initiated by H-bond rupture between the 4-keto group of the  $\beta_1$ -ring and neighbouring residues Y201 and W288<sup>10,15–20</sup>. Several different proposals have been made for the primary photochemistry resulting in this particular H-bond rupture: (1) a charge transfer state<sup>21</sup>; (2) a shift in keto–enol equilibrium<sup>17</sup>; (3) a transfer of vibrational energy from the carotenoid to the protein leading to the H-bond rupture<sup>22</sup>, similar to H-bond rupture in bacteriorhodopsin<sup>23</sup>; (4) a structurally distorted form of the carotenoid in the S1 state characterized by increased carotenoid planarity<sup>18</sup>; (5) a photoinduced s-isomerization of the C6–C7 single bond, flipping the orientation of the  $\beta_1$ -ring by 90°<sup>10</sup>.

Support for s-isomerization in OCP stemmed from the X-ray structure of the isolated NTD (also known as red carotenoid protein, RCP), in which the keto-carotenoid was present in a C6–C7 *s-cis* conformation<sup>10</sup>, and frequency calculations showing agreement between a C6–C7 *s-cis* conformation and  $OCP^R$  Resonance Raman data<sup>21</sup>. However, the hypothesis for s-isomerization in  $OCP^R$  is not consistent with recent infra-red (IR) anisotropy observations<sup>18</sup>. A recent study of the fluorescence spectra and yields of  $OCP^0$  with different carotenoids suggested that the mechanism of OCP photoactivation does not involve the keto group of the  $\beta_1$  ring but includes out-of-plane motions of the  $\beta_2$  ring<sup>24</sup>. In the photoreceptor, rhodopsin, its photosensing pigment, retinal, which is synthesized from a carotenoid by irreversible oxidative cleavage<sup>25</sup>, undergoes an “aborted” bicycle pedal<sup>26</sup> (BP) double bond rotation as part of vision photokinetics<sup>27</sup>. During this process BP motion is observed as part of the S1 relaxation, while one of the two reacting double bonds rotate back during S0 relaxation<sup>28,29</sup>. Such a photoresponse, however, has never been proposed for OCP. Here, we show time resolved crystallographic and spectroscopic evidence that resolves the initial

**Table 1 | Comparison of canthaxanthin dihedral angles observed in OCP structures in the three states: Dark, I1 and I4. Dihedral angles were measured using atomic PDB coordinates for carbon atoms**

	Dark (this study)	1 m (this study)	10 m (this study)	Syn OCP <sub>CAN</sub> (4XB5)	Syn OCP <sub>ECH</sub> (5TUX)	Arth OCP <sub>HECH</sub> (5UI2 -CA)	Arth OCP <sub>HECH</sub> (5UI2 -CB)
C5-C6-C7-C8 (β1 ring)	<b>153</b>	<b>157.8</b>	<b>-35.6</b>	116.3	131.8	118.5	131.9
C6-C7-C8-C9	160	163.1	159.9	175.4	176.7	172.8	174.7
C7-C8-C9-C10	167	160.4	167	-155.3	-168.7	-163.7	-176.8
C8-C9-C10-C11	164.9	162.4	164.9	175.8	174.9	177.9	171.1
C9-C10-C11-C12	-176.1	-166.1	-176.2	178.8	-179.5	165.2	173.6
C10-C11-C12-C13	176.9	-172.8	177.0	174.4	173.7	175.4	175.5
C11-C12-C13-C14	177.6	163	177.7	167.8	170	177.5	175.9
C12-C13-C14-C15	172.7	175.4	172.7	173	172.8	171	170
C13-C14-C15-C15'	175	-176.2	175	-171.4	177.8	-175.7	171.5
C14-C15-C15'-C14'	172.4	144.9	172.4	172.7	171.8	170.7	171.4
C15-C15'-C14'-C13'	-175.2	163.8	-175.2	169.8	-178.7	179.6	-168.2
C15'-C14'-C13'-C12'	171.5	-177.5	171.5	173	172.2	172.8	169.8
C14'-C13'-C12'-C11'	-170.9	-148.1	-170.9	-153.3	-165.9	-161.6	171.4
C13'-C12'-C11'-C10'	172	171	172	173.1	172.8	174.8	170.9
C12'-C11'-C10'-C9'	-175.9	167.5	-175.9	171.9	-179.2	170.3	-158.8
C11'-C10'-C9'-C8'	172.9	173.3	172.8	175.2	174.8	174	-179.7
C10'-C9'-C8'-C7'	<b>178.4</b>	<b>-23</b>	<b>178.3</b>	-160.3	-175.1	-170.2	174.9
C9'-C8'-C7'-C6'	<b>176.3</b>	<b>-171.6</b>	<b>176.3</b>	177.6	178.5	177.3	178.6
C8'-C7'-C6'-C5' (β2 ring)	<b>-45.3</b>	<b>145.1</b>	<b>-45.3</b>	-72.1	-58.6	-66	-51.9
RMSD	0.436	0.706	0.436				

Dihedral angles undergoing substantial change upon illumination are highlighted in bold.

RMSD was calculated with Pymol Align using PDB entry 4XB5 as a target selection.

Deposited dihedral angles for CAN-binding (PDB entry 4XB5), ECN-binding (5TUX), and 3'-hECN-binding (5UI2) OCPs are also included for comparison.

photoproducts and subsequent structural propagation in the OCP activation process.

## Results

### OCP<sup>0</sup> crystal structure and photoresponse

Figure 1b shows the light-induced absorption changes measured in crystals and solutions of OCP. In contrast to a previous crystallographic investigation of OCP photoactivation<sup>17</sup>, we observe that the absorbance spectra of OCP<sup>0</sup> in solution and in crystals are nearly identical (Fig. 1b), thereby providing evidence for the same electronic structure of the carotenoid in both crystals and solution. Illumination of crystals with 410 nm light and 3.5 mWcm<sup>-2</sup> power density causes a significant spectral red-shift of 25 nm due to OCP<sup>0</sup>-OCP<sup>R</sup> conversion within 5 min on average (Fig. 1b insert). In solution, a similar spectral shift is observed: it occurs on the same timescale as in crystals, but slightly faster (3 min), as resolved from the detailed spectroscopic analysis described later in the manuscript. Strong similarities between the photoresponses in the crystals and in solution therefore allow us to conclude that OCP is photoactive in crystals with very similar photoresponse characteristics as seen in solution.

An early reaction intermediate was captured by intense illumination and cryo-trapping of OCP crystals. The crystal structure and carotenoid conformation were determined at 1.3 Å resolution for the dark state (OCP<sup>0</sup>, Fig. 1a, Supplementary Table 1) and found to be in good agreement with those reported in previous X-ray studies<sup>9,10,15,17</sup> (Table 1).

The data furthermore supports identification of glycerol, acetate, the Cl<sup>-</sup> ion and 401 water molecules in the crystal structure (Fig. 2 and Supplementary Tables 2, 3). The location of Cl<sup>-</sup> in this study was confirmed by long-wavelength X-ray crystallography (Fig. 2 and

Supplementary Table 3). In brief, the contribution of Cl<sup>-</sup> to the anomalous scattering signal at 2.9 keV is 3.95 e<sup>-</sup> (f<sup>0</sup>), whereas at 2.8 keV, this value is 0.40 e<sup>-</sup> (f<sup>0</sup>). The difference between these two values allows for specific sites of Cl to be identified by observing the anomalous difference Fourier map at the expected Cl site for each (Fig. 2b). Cl<sup>-</sup> is resolved in the CTD, where it coordinates four water molecules through ion-dipole interactions at distances of 3.0–3.2 Å (HOH16, HOH23, and HOH46) and 4.0 Å (HOH41). The closest CAN carbon is C12, located at 4.1 Å distance from the Cl<sup>-</sup> ion in the CTD (Fig. 2a). Three amino acids (L248, T275, and P276) are within 4 Å distance from Cl<sup>-</sup>. The electron density assigned to the Cl<sup>-</sup> ion, was attribute—to Cl<sup>-</sup> in the first OCP crystal structure (PDB entry 5UI2) based on the signal intensity and crystallization conditions<sup>9</sup>, but subsequently has been assigned to a water molecule in several reports: HOH609 (PDB entry 5TV0), HOH699 (PDB entry 5TUX), HOH673 (PDB entry 4XB5), and HOH1020 (PDB entry 3MG1).

### Unravelling s-BP isomerization as the first photoproduct

In addition to OCP<sup>0</sup>, X-ray crystallography data was collected of four illuminated structural intermediates I1, I2, I3, and I4 corresponding to 1, 2, 5, and 10 min of illumination. Data collection and refinement statistics were comparable to that of the OCP<sup>0</sup> reference data. Q-weighted F<sub>Light</sub>-F<sub>Dark</sub> difference electron density (DED) maps<sup>30</sup>, indicating light-induced changes in X-ray data, and CAN coordinates at different time points (see “Methods”, Fig. 3) are presented in Fig. 1c. The coordinates for the partially occupied illuminated state (I1–I4, Fig. 1c) were resolved through their refinement to extrapolated structure factors based on the approach described previously<sup>31</sup>. The I1 dataset with 1 min illumination reveals *s-trans* to *s-cis* CAN isomerization along the C9'-C8' single bond concerted with *s-cis* to *s-trans* isomerization along the

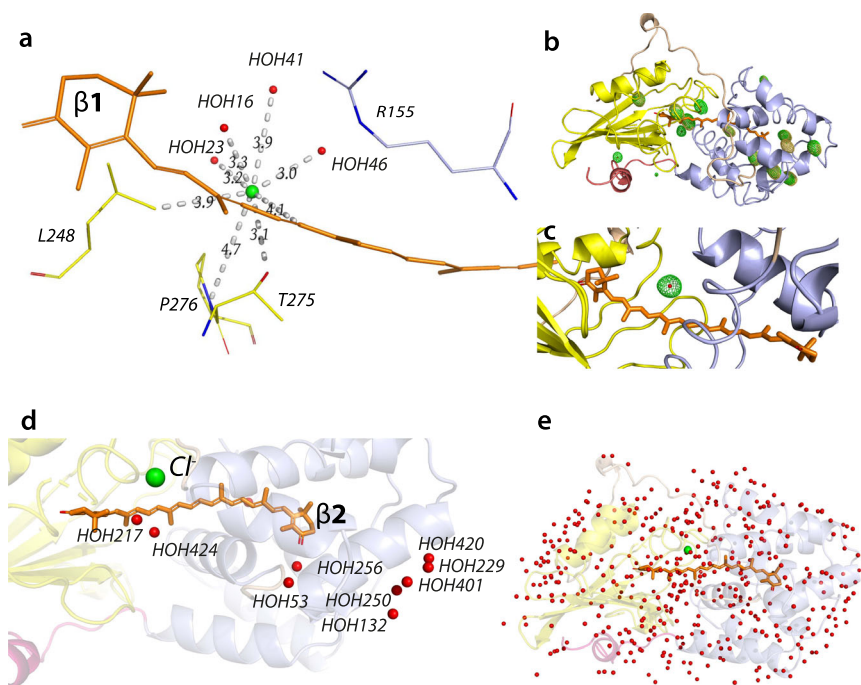


**Fig. 2 | Identifying Cl<sup>-</sup> location.** **a** Cl<sup>-</sup> (green sphere) is resolved in the CTD using Long-wavelength experiment for Cl<sup>-</sup> identification. Cl<sup>-</sup> coordinates four water molecules (red spheres) through ion-dipole interactions at distances of 3.0–3.2 Å (HOH16, HOH23, and HOH46) and 4.0 Å (HOH41). **b** Overall structure anomalous difference density Fourier maps at 2.9 keV (green) and 2.8 keV (light orange). The regions where green density is present and light orange density where it is absent indicate the presence of Cl (red dot). In the instances where the Cl atom could not

be modelled due to a sigma greater than 6, dummy atoms have been placed to indicate the potential location (dots). **c** Close-up view of the modelled Cl<sup>-</sup> site (red dot) with the 2.9 keV anomalous difference Fourier map density surrounding it (green). **d** The newly identified water molecules as described in Supplementary Table 2. **e** A total of 401 water molecules (red spheres) were resolved in the OCP structure reported herein.

C7'-C6' single bond (s-BP isomerization) as the early step of activation (Fig. 1c, d and below). As a result, C8' = C7' changes its orientation (Fig. 1c, d). The isomerization-related DED signals are also detected in I2, though less pronounced compared to I1. In contrast to I1 the resolved extrapolated coordinates of I2 support only a minor population of the concerted C9'-C8' *cis*/ C7'-C6' *trans* state while the dark (C9'-C8' *trans*/ C7'-C6' *cis*) conformation becomes again the dominant state. The crystallographic observations for the first 2 min of illumination go in line with the kinetics and spectra determined by solution spectroscopy described below and identify the bicycle pedal (s-BP) isomerization. Unlike the double-bond BP<sup>26</sup> mechanism driving the first steps of vision in rhodopsin retinal, the photoresponse observed in OCP involves a single bond s-BP mechanism that has not been reported before. It occurs with  $k_{\text{isom}} = 0.0263 \text{ s}^{-1}$  and is followed by thermal relaxation ( $k_{\text{therm}} = 0.0062 \text{ s}^{-1}$ , Fig. 1d). The isomerization fully decays after 5 min in I3 and I4, judging from DED maps, 2mFo-DFc maps, and refined coordinates using extrapolated structure factors (Fig. 1c and Table 1).

The refined coordinates obtained from extrapolated structure factors identify the CAN s-BP isomerization after 1 min of illumination at the experimental light intensity as a first light-activation step. UV/Vis spectroscopy then confirms that the rate of its accumulation is proportional to the illumination intensity (Supplementary Fig. 1a–c). Complete thermal relaxation of CAN back to its dark conformation occurs after 5 min of illumination but also in darkness (Supplementary Fig. 1a and Supplementary Note 1), indicating that the process is thermally-driven and proceeds efficiently at ambient temperature. In contrast to the current prevailing model<sup>10,15–20</sup>, which proposes a H-bond rupture in the CTD as the primary photoproduct of the OCP photocycle, our X-ray data directly demonstrate that a transient s-BP single bond isomerization occurs prior to rearrangements in CTD. This finding reveals the molecular activation mechanism that precedes the

formation of the product state previously described<sup>10,15–20</sup>. The I1 structure is the first example where s-BP isomerization of a carotenoid carbon chain regulates the activity or the biological function of a protein. The BP reaction in general is a volume-conserving process and was demonstrated to be favourable in a tight-protein cavity<sup>28,32</sup> or other restraining environment<sup>33</sup>.

#### Photoinduced structural rearrangements in I1–I4

Photoinduced structural changes occur throughout the OCP protein and propagate in a time-dependent manner. The  $F_{\text{I1}}-F_{\text{Dark}}$  map reproducibly shows differences in three regions (Fig. 3 and below): in the NTD with the highest DED amplitudes within 6 Å from the CAN  $\beta 2$  ring (Zone 1, Fig. 5) and in the N-terminal extension (Zone 2, Fig. 5). The DED signals appear in the CTD (Zone 3, Fig. 3 and below) with time delays longer than 1 min. In the I2 intermediate (i.e., after 2 min of illumination), the DED signals appear primarily in the region of the CAN binding pocket and subsequently appear along helices of the CTD in the I3 and I4 structures (below). Concomitant with the development of DED signals in the CTD, the DED signals in Zones 1 and 2 decay in I3 and I4. These results indicate that NTD is the primary site of action in OCP light-activation. Therefore, the initiation of photo-sensing in the OCP photocycle involves structural changes in the NTD rather than in the CTD as previously suggested<sup>17</sup>. The areas where we observe DED signals due to the light-induced changes also demonstrate B factors increase (Figs. 4, 5).

The structural rearrangements in the intermediates I1, I2, I3, and I4 are analyzed in detail following coordinate refinement using extrapolated structure factors. Tyrosine Y44 and tryptophan W110 are located in closest proximity (4 Å) to the C6'-C7' = C8'-C9' moiety in the hydrophobic pocket which also contains the  $\beta 2$ -ring of the carotenoid (Fig. 6a). Together with W41, residues Y44 and W110 interact with the carotenoid  $\beta 2$ -ring through  $\pi$ - $\pi$  stacking (Fig. 1a)<sup>15</sup>. In the I1 structure,



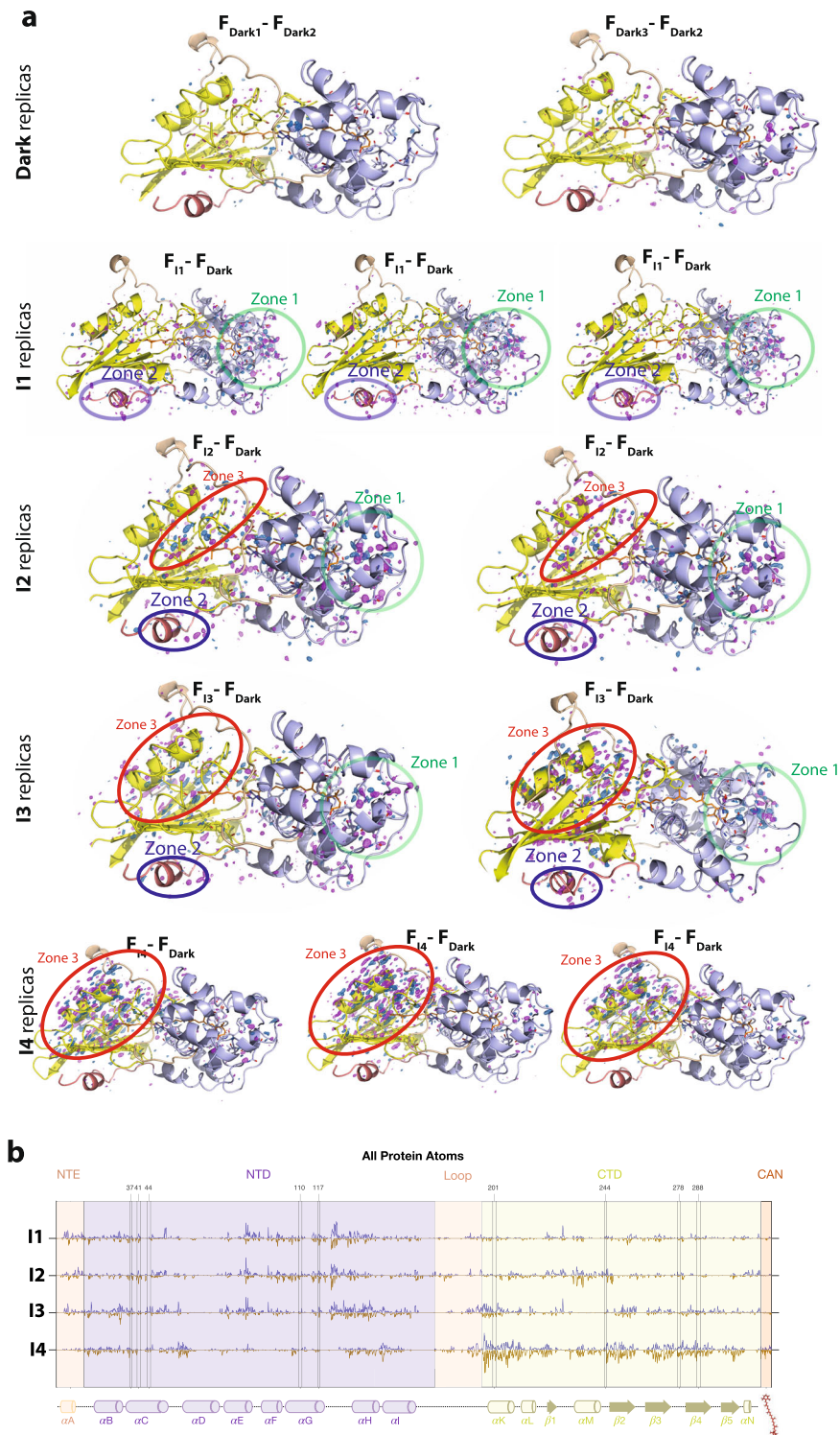


**Fig. 3 | DED signals in different states.** **a** DED maps contoured at  $\pm 3.5\sigma$  (blue and magenta) correspond to the appearance and disappearance of density, contoured at  $3.5\sigma$ . Dark state DED signals contoured at  $(\pm)3.5\sigma$ . The  $F_{\text{Dark1}}-F_{\text{Dark2}}$  and  $F_{\text{Dark3}}-F_{\text{Dark2}}$  exhibit marginal DED signals. The  $F_{\text{I1}}-F_{\text{Dark}}$ ,  $F_{\text{I2}}-F_{\text{Dark}}$ ,  $F_{\text{I3}}-F_{\text{Dark}}$ , and  $F_{\text{I4}}-F_{\text{Dark}}$  datasets show reproducible strong DED signals in the three different

zones. The following domains undergoing photoinduced conformational changes are represented in oval shapes: Zones 1 (NTD), Zones 2 (NTE), and Zones 3 (Alpha-helices in CTD). **b** Difference electron density amplitudes calculated as described in the X-ray data refinement section of the “Methods”.

no changes of coordinates are observed for W110 compared to  $\text{OCP}^{\text{O}}$  but the Y44 sidechain undergoes a rotation by  $31^\circ$  (Fig. 6a). This observation suggests that the Y44 sidechain reacts to the s-BP isomerization to trigger structural changes in NTD. The structures of the I1 and I2 intermediates suggest that the repositioning of the Y44 sidechain causes the displacement of multiple amino acids in NTD.

These, among many others, include residues Y111 and G114, which are closest to Y44 and are displaced in I1 and I2 (Fig. 6a). In agreement with our crystallographic observations, previous spectroscopic analysis demonstrated that the Y44S mutation fully inhibits  $\text{OCP}^{\text{O}}-\text{OCP}^{\text{R}}$  conversion<sup>20</sup>. As a result of Y44 rotation by  $31^\circ$  in NTD in the I1 state, the distance between the hydroxyl group of Y44 and the C9' carbon

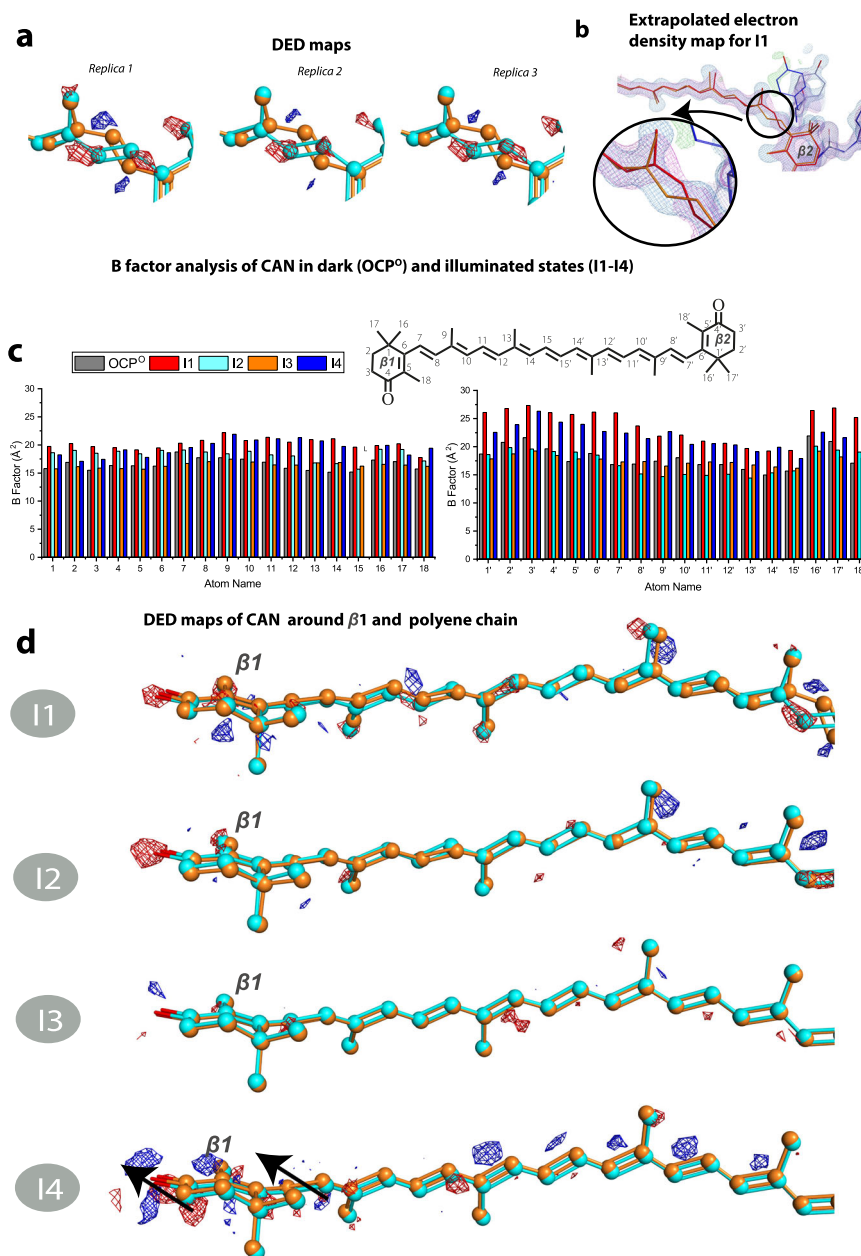


**Fig. 4 | CAN conformation upon illumination.** **a** Reproducibility of isomerization signal. Similar DED signals assigned to isomerization were observed for three different I1 datasets. **b** Extrapolated maps and coordinates of CAN.

**c** Atomic B factors for CAN comparing the OCP<sup>0</sup> (dark) structure to the photo-product states in I1, I2, I3, and I4. **d** DED signals around  $\beta$ 1-ring and polyene chain of CAN in I1-I4 states.

reduces by 2.0Å, redistributing charge-density around C9'-C8' (Supplementary Fig. 1d, e). These changes are transient and the residues return to their original location as in OCP<sup>0</sup> after 5–10 min of continuous illumination (Fig. 6a). Leucine L37, which has been proposed to play an important role in OCP light-activation<sup>24</sup>, does not undergo any significant movement upon illumination (Fig. 6a). We therefore conclude that the s-BP isomerization of CAN in I1 causes rearrangement of the CAN  $\beta$ 2-ring binding pocket in the NTD, which is mediated by contact with Y44.

The rearrangement of the  $\beta$ 2-ring binding pocket coincides with further conformational changes within the NTE and the NTD. This affects primarily helices  $\alpha$ A- $\alpha$ C and  $\alpha$ E- $\alpha$ H, as can be judged from the location of DED signals (Fig. 5). The amplitude of these signals is maximal after a 1 min illumination ( $F_{I1} - F_{Dark}$ ) followed by a decrease after a 2 min illumination ( $F_{I3} - F_{Dark}$ ) and complete decay after a 10 min illumination ( $F_{I4} - F_{Dark}$ ). The conformational rearrangements

of the  $\alpha$ A- $\alpha$ C and the  $\alpha$ E- $\alpha$ H helices affect the hydrogen-bond network by increasing the number of polar contacts in the main backbone of I1 by 5% compared to OCP<sup>0</sup>. In I1, 14 new H-bonds are created in the backbone which gradually decay in I2–I4 (Supplementary Table 4). These results indicate that, following light-activation, the light-sensing process in OCP is mediated not only by the CAN  $\beta$ 2-ring binding pocket but involves the hydrogen-bonding of the whole domain.

The DED signals within a 5Å radius from the carotenoid at the CTD and NTD interface (Fig. 5) are assigned to modification of the salt bridge between R155, E244 (Fig. 6b) and the reorganization of water molecules (Figs. 6b, 7). The salt bridge rupture between R155 and E244 is already observed in I1 and increases the distance between residues E244 and R155 by 1Å (Fig. 6b). The position of R155 is affected by the water molecules HOH41 and HOH46 through H-bonding (Fig. 6b and Supplementary Fig. 2a). The positions of the Cl<sup>-</sup> anion, HOH41, HOH46, and other water molecules in the water channels are rearranged during

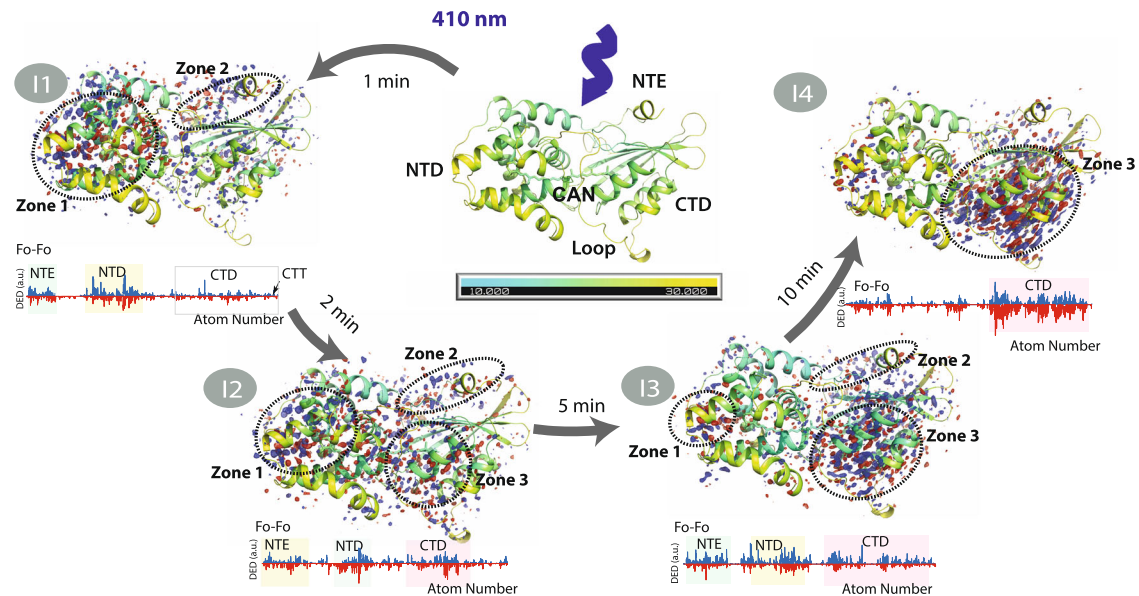


**Fig. 5 | Overall structural effect of illumination on OCP structure.** Datasets from which all images are derived (Dark, I1–I4) have a resolution of 1.3–1.4 Å (Supplementary Table 1) and time points at which crystals were cryo-trapped are indicated for I1–I4. Each structure is coloured in cyan-yellow gradient based on B-factor (10.0 (cyan)–30.0 (yellow)). (I1–I4, upper panel)  $F_0 - F_0$  Difference electron density (DED) maps (blue/red at  $\pm 3.5\sigma$ ) for the four states are shown below each corresponding structure: (I1) 1 min ( $F_{I1} - F_{\text{Dark}}$ ), (I2) 2 min ( $F_{I2} - F_{\text{Dark}}$ ), (I3) 5 min ( $F_{I3} - F_{\text{Dark}}$ ) and (I4) 10 min ( $F_{I4} - F_{\text{Dark}}$ ). The DED signals are localized in

the three major areas: *zone 1*: NTD; *zone 2*: NTE; *zone 3*: alpha-helices in CTD. Note that some DED signals are observed at the interface between the two domains (red arrows in I1 and I2), while the C-terminal tail (CTT) does not exhibit any noticeable DED signal. Red: negative DED, blue: positive DED on the  $-3.5\sigma/3.5\sigma$  contour levels, respectively. See main text for further explanation. (I1–I4, lower panel) DED signals are also shown as integrated signals<sup>33</sup> around each atom in the protein chain. The figure was created using PyMOL Molecular Graphics System (Version 2.5.0).

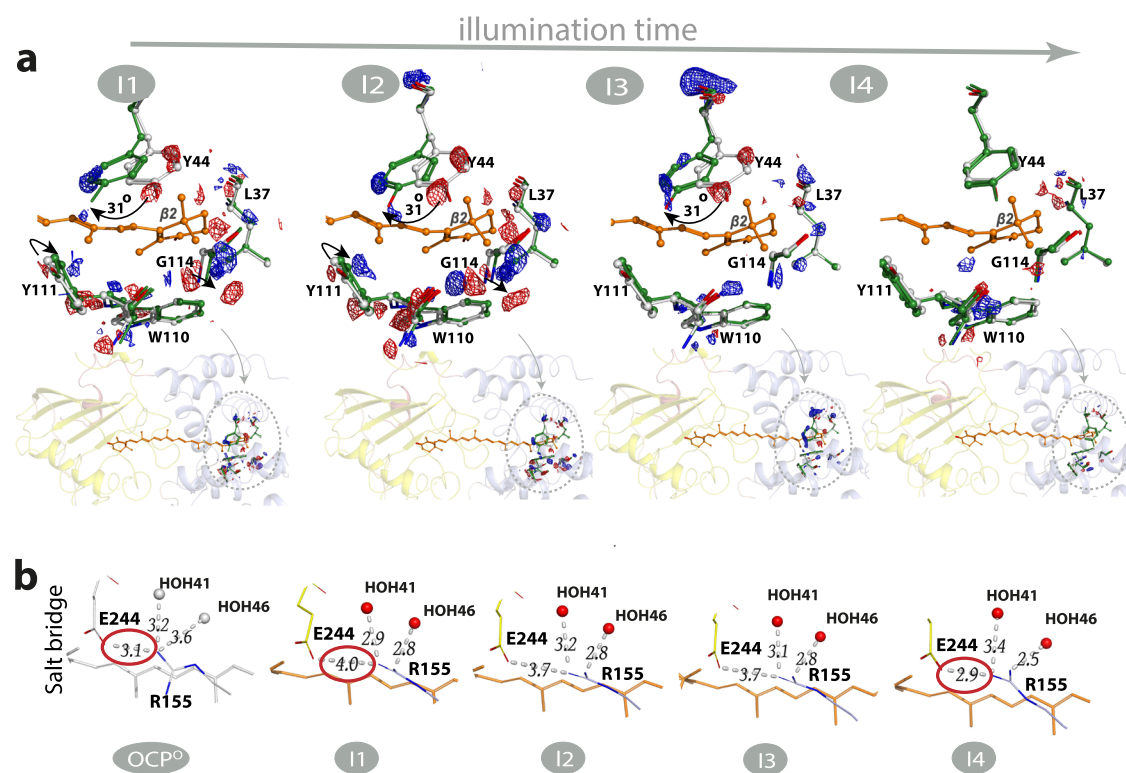


**Fig. 6 | OCP structural changes in I1–I4 states upon illumination.** **a** Dark ( $\text{OCP}^0$ ) coordinates are represented by grey sticks while light state coordinates obtained from extrapolated maps (I1–I4) are represented by green (NTD) and orange (CAN)

sticks. Difference electron density (DED)  $F_{\text{Light}} - F_{\text{Dark}}$  are shown with blue/red mesh at  $\pm 3.0\sigma$ . **b** Changes in the salt bridge formed between residues E244 and R155. The figure was created using PyMOL Molecular Graphics System (Version 2.5.0).



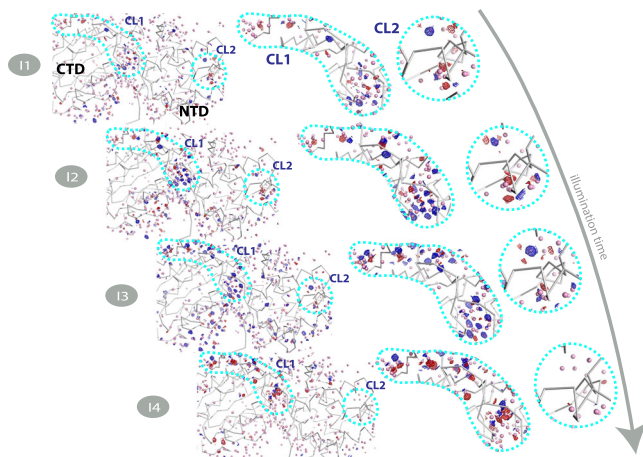


**Fig. 7 | Light-driven water molecules redistribution in the OCP crystal structures.** Q-weighted DED maps associated with the four pairs I1, I2, I3, and I4 (in blue and red, contoured at  $\pm 3.0\sigma$ ). Amino acids are represented by grey ribbons, while water molecules are shown as pink spheres respectively. CL1 and CL2 indicate water clusters.

the illumination period (Supplementary Fig. 2, Figs. 6b, 7). The movement of the Cl<sup>-</sup> anion observed in the first 5 min of illumination (I1–I3) is likely caused by the H-bond rearrangement in the water channel (CL1 in Fig. 7, Supplementary Fig. 2a and Supplementary Note 2), while in I4 it is proposed to result from translocation of the CTD away from NTD (Supplementary Fig. 2b).

In the final illumination product (I4, Fig. 6b) the distance between residues E244 and R155 is restored to the original 3 Å distance found in the dark state, suggesting that, although an important event in the initial steps of light activation, salt-bridge rupture may not be a prerequisite for subsequent domain separation. Previously reported FTIR and X-ray protein footprinting results suggested that signal propagation of OCP conformational change is mediated by rearrangement of internal hydrogen bonding networks<sup>11,34</sup>. We complement this knowledge by showing that salt bridge rupture between R155 and E244, the important precursor of NTD and CTD separation, occurs in the first illumination step (I1) and is controlled by a hydrogen bonding network involving protein-bound water molecules.

In addition, an increase in DED signal intensities in the CTD is observed with increasing illumination time (Zone 3, Fig. 5). This is first manifested in CTD amino acids L248 and T275 among others located at the interface of CTD and NTD (Supplementary Fig. 2a). The DED signals for the CTD (Fig. 5) do not represent a complete domain rearrangement but rather a rigid-body motion of the CTD domain in the direction away from the NTD and the dimer interface (Supplementary Fig. 2b) similar to that previously reported<sup>17</sup>. This CTD translocation, which was previously observed and seems to be a prerequisite for H-bond disruption<sup>17</sup>, is only observed at longer illumination times in our data (after 5–10 min, Supplementary Fig. 2) and only after rearrangement of the NTD binding pocket. Therefore, we propose that the H-bond rupture represents a secondary effect caused by domain separation and it is not a photo-driven process as previously proposed<sup>17,18</sup>.

### FTIR and UV/Vis spectroscopy in solution

We next performed FTIR and UV/Vis spectroscopy in solution using the same illumination conditions as for crystals in order to confirm that CAN isomerization is photoinduced (Fig. 8) and determine whether the same photoactivation reactions observed in crystals also take place in solution. Figure 8 displays the results from the combined global analysis fits of the UV/Vis and FTIR data using a well-established approach to analyze time-resolved spectroscopic data, which yields Evolution-

Associated Spectra (EAS) components<sup>35–37</sup>. Since the experiment in this study was performed under continuous illumination, the EAS components do not represent intrinsic lifetimes of the intermediate states but rather dissected population accumulation rates at given illumination power densities (Supplementary Fig. 1a–c). Four components of spectral regions (EAS1–4) are identified to describe the absorbance changes in both UV/Vis and IR spectra with lifetimes of 13 s, 38 s, 162 s and a steady-state component (infinity). Note that the time acquisition rate of FTIR is below the EAS1 rise-time, EAS1 FTIR spectra cannot be resolved. The concentration profiles of EAS components in time are presented in Fig. 8c, insert.

The overall photocycle kinetics in OCP solution and OCP crystals are very similar (Figs. 1b, 8a and justification below). Therefore, the contribution of each component (EAS) in I1–I4 states should be approximately as follows: (i) I1 state: EAS1 (3%), EAS2 (40%) and EAS3 (57%), (ii) I2 –EAS2 (13%) and EAS3 (87%), (iii) I3 –EAS2 (2%) and EAS3 (98%) and (iv) I4 –EAS3 –100%. Note that the absence of the final component EAS4 in crystals is probably due to crystal packing constraints on side-chain conformational dynamics so it was excluded from the population estimates (see the justification below). The first component (EAS1) exhibits a positive and a negative spectral signature in the visible region (Fig. 8a, grey solid line) peaking at 475 and 550 nm respectively. We assign this spectrum to the equilibration process between OCP<sup>0</sup> and the newly forming intermediate species EAS2. EAS2 (at 38 s) has a very similar visible spectrum to OCP<sup>0</sup> ( $t_0$  spectra) though like OCP<sup>8</sup> it has more red shifted absorption peaking at 575 nm, which decreases the bleach at 470 nm (Fig. 8b, black line). But unlike in OCP<sup>8</sup>, the red shift of the spectrum is much less pronounced in EAS2.

The comparison of EAS2 and OCP<sup>0</sup> shows an increased absorbance at 350 nm (black solid line, Fig. 8b) of EAS2. This 350-nm band yields the so-called ‘cis-peak’, a characteristic signature of *trans-cis* isomerization in carotenoids<sup>38,39</sup>. The IR spectrum of the corresponding EAS2 component in D<sub>2</sub>O buffer shows positive bands in the 1655–1641 cm<sup>-1</sup> region while exhibiting a negative band at 1540–1550 cm<sup>-1</sup> (Fig. 8c, red solid line). The positive band corresponds to the amide I signal. The position of the 1542–1550 cm<sup>-1</sup> bleach is insensitive to D<sub>2</sub>O/H<sub>2</sub>O exchange (Supplementary Fig. 1f, red solid line) and agrees with the frequency of C=C stretches in canthaxanthin<sup>40</sup> and other carotenoids<sup>41</sup>. In carotenoids, the oscillator strength of C=C stretches is known to be affected upon C=C reorientation or reorganization<sup>42</sup>. Therefore, the presence of the 1542–1550 cm<sup>-1</sup> bleach in the EAS2 component could be a signature of CAN s-BP isomerization as seen in Fig. 1c in I1. The EAS3 component confirms that s-BP isomerization is a transient 2.5 min phenomenon leading to a ‘relaxed’ state where C9’-C8’ and C7’-C6’ single bonds are back in *trans* and *cis* conformations, respectively, as can be concluded from a decrease of the 1542 cm<sup>-1</sup> bleach (162-s, Fig. 8c, blue dotted line). An additional UV/Vis measurement with a shorter illumination period confirms that the relaxation of the two concerted isomerization steps is thermally driven (Supplementary Fig. 1a, see Supplementary Note 1 for the detailed explanation). To support the FTIR assignments, we also performed harmonic frequency calculations of CAN in the dark conformation (CAN<sub>Dark</sub>) and in the s-BP isomer (CAN<sub>I1</sub>) using the carotenoid coordinates from Fig. 1c after optimisation using redundant coordinates (Fig. 8d). The major frequency of the C=C stretches coupled with the C=O stretches in CAN<sub>Dark</sub> is 1542 cm<sup>-1</sup> (Fig. 8d, cyan sticks), while in the CAN<sub>I1</sub> state, its oscillator strength decreases and its frequency redshifts to 1550 cm<sup>-1</sup> (Fig. 8d, orange sticks). The resulting calculated difference signal (CAN<sub>I1</sub>-CAN<sub>Dark</sub>) is characterized by the 1542 cm<sup>-1</sup> bleach (Fig. 8d, red dotted line). Our spectroscopic results on OCP solution, supported by frequency calculations, thus confirm that s-BP single bond isomerization is a light-driven process occurring also in physiological conditions.

Here we report photokinetics of OCP with CAN, but OCP has been shown to bind and be active with various keto-carotenoids (3’-



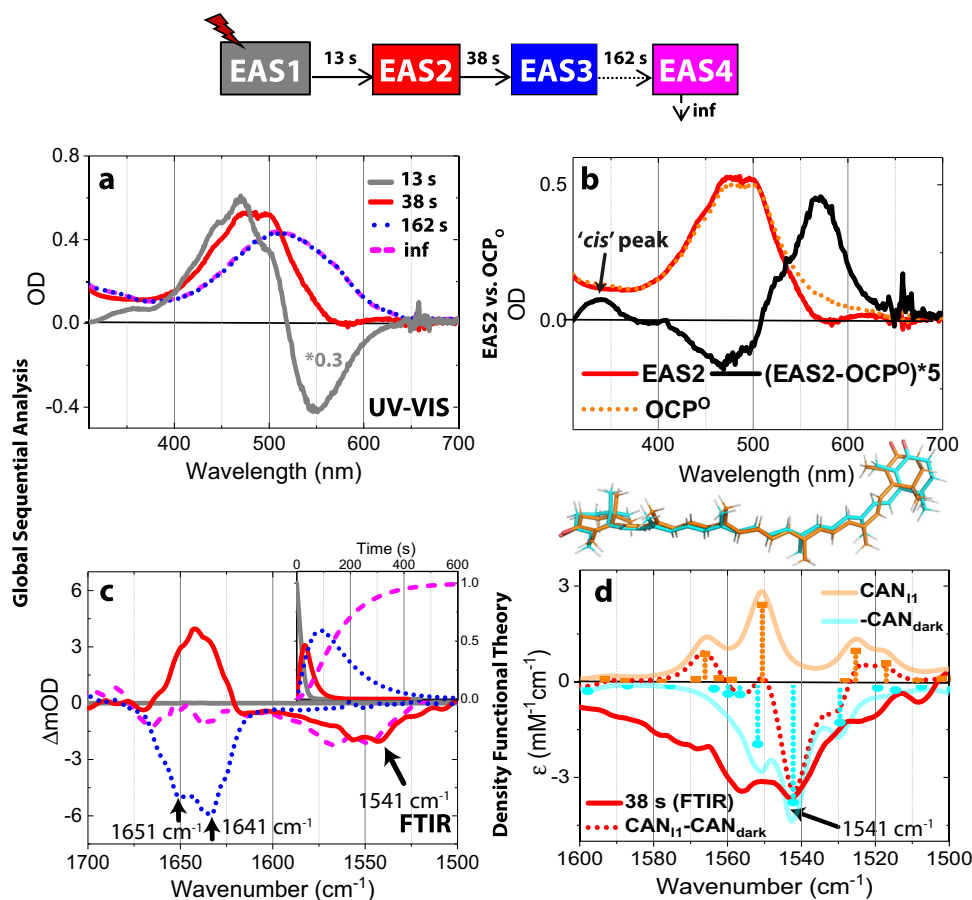


**Fig. 8 | Spectroscopic evidence for bicycle pedal isomerization in OCP in solution.** Results of the simultaneous global fit of UV-VIS (a) and FTIR (c) data upon 10 min of illumination. The kinetic model used for the fit is shown on top of the panel with the respective lifetime for each transition between intermediates. The same colour code is used for the corresponding EAS components in panels (a and c). Refer to the main text for an explanation of the relationship between the resolved EAS and the illuminated structural intermediates II–I4 (Figs. 1c, 6). **a** UV-VIS EAS. For EAS1 spectrum multiplication a factor of 0.3 was used. **b** EAS2 component was compared to the original OCP<sup>0</sup> spectrum. **c** FTIR EAS (in D<sub>2</sub>O); FTIR

(in H<sub>2</sub>O) is shown in Supplementary Fig. 1f. Insert: Relative concentration profiles for each EAS. **d** Theoretical IR frequencies and intensities were calculated using harmonic frequency calculations (HFC) at the B3LYP/6-311+G level. IR values were calculated for CAN in the two (CAN<sub>dark</sub> and CAN<sub>I1</sub>) states using CAN coordinates extracted from the extrapolated maps. Theoretical IR frequencies and calculated FTIR spectra are presented by sticks and solid lines respectively. Optimized CAN coordinates from HFC are shown on top of the panel. CAN<sub>I1</sub>-CAN<sub>dark</sub> (red dotted line) obtained from HFC agree with the 1542 cm<sup>-1</sup> bleach from the 38-s EAS2 (red solid line). Source data are provided as a Source Data file.

hydroxyechinenone, 3'-hECN; echinenone, ECN; as well as CAN)<sup>10,17,43</sup>. The 350 nm peak observed here was previously reported in various carotenoids<sup>38,39</sup>, therefore it could be a s-BP isomerization signature in all OCP keto-carotenoid constructs. The position and oscillation strength of C=C stretch is carotenoid-specific: the 1542–1550 cm<sup>-1</sup> bleach observed here is unique for CAN and is observed in ECH at lower amplitude and higher frequencies<sup>44</sup>.

The EAS2 component also contains positive amide-I FTIR signals peaking at 1651 cm<sup>-1</sup> and 1641 cm<sup>-1</sup> which subsequently bleach in later stages (EAS3, Fig. 8c, blue dotted line). These signals, assigned to amide-I peaks based on previously reported IR signals of OCP WT and mutants<sup>8</sup>, are indicative of H-bond rearrangements which are seen in the II crystal structure (Supplementary Table 4). The positive amide-I FTIR signals can be assigned to the new polar contacts appearing in II (EAS2, 38 s, Fig. 8c). Negative amide-I FTIR signals in the EAS3 component indicate the loss of these polar contacts as seen in I4 (Supplementary Table 4).

In line with previous studies<sup>13,18,34</sup> the absorption peak at 1651 cm<sup>-1</sup> is insensitive to D<sub>2</sub>O/H<sub>2</sub>O exchange, unlike that at 1645 cm<sup>-1</sup> (Fig. 8c and Supplementary Fig. 1g, Supplementary Note 3). We have therefore tentatively assigned the 1651 and 1641 cm<sup>-1</sup> (D<sub>2</sub>O)/1645 cm<sup>-1</sup> (H<sub>2</sub>O) bands to a buried  $\alpha$ -helix and to a solvent exposed  $\alpha$ -helix of NTD respectively.

In agreement with<sup>34</sup> we tentatively assign ~1600–1645 cm<sup>-1</sup> shoulder in FTIR (in H<sub>2</sub>O) to vibrational motions of HOH (Supplementary Fig. 1f). See Supplementary Note 3 for more details regarding the contribution of water molecules to FTIR data. In support of this assignment in Supplementary Fig. 1f, we observed that the presence of the 1600–1640 cm<sup>-1</sup> band in the H<sub>2</sub>O data (Supplementary Fig. 1f- EAS2 and EAS3) correlates with the light-driven displacement of water molecules observed in the crystallographic data on the same time scale (Fig. 7, Supplementary Fig. 2- I2 and I3). The rearrangement of water molecules affects the two water clusters CL1 and CL2 each centred on HOH46 and HOH152 respectively. The strongest DED signals are observed in CL1, which is located on the interface between the two domains (Fig. 7).

Contrary to a previous suggestion<sup>34</sup>, our data does not support involvement of the C-terminal tail to changes of the 1645 cm<sup>-1</sup> peak, since no structural rearrangements are observed in this region, as can be judged from DED maps and DED amplitudes in the crystallographic data corresponding to the same time delays (II–I2, Figs. 3b, 5). In line with the final I4 crystal structure, where the CTD translocates away from the NTD without CTD rearrangement, we do not observe CTD characteristic  $\beta$ -sheet-related FTIR signals in the 1640–1600 cm<sup>-1</sup> region (Fig. 8c, violet dashed line). Since, as was shown previously<sup>10,11</sup> the process of domain separation occurs without substantial unfolding

of the secondary structure, we observe very low amplitude of the FTIR signals in the amide I region (1640–1660  $\text{cm}^{-1}$ ). The EAS4 (infinity/steady-state) therefore represents complete dissociation of the CTD and NTD<sup>11</sup>, which is not observable in the crystallographic data due to the crystal packing constraints<sup>17</sup>. Furthermore, the bleach around 1550–1575  $\text{cm}^{-1}$  of EAS4 (Fig. 8c, violet dashed line) is indicative of C=C bond changes and supporting the isomerization process. This is in agreement with a previous study in which C6–C7 *s-cis* CAN was observed in RCP<sup>10</sup>. RCP is a truncated OCP fragment that is assumed to be a native OCP<sup>R</sup> state after domain separation<sup>10</sup>. To confirm our 1550–1575  $\text{cm}^{-1}$  bleach assignment, we also performed harmonic frequency calculations (HFC) at the B3LYP/6-311+G level of IR spectra for CAN carotenoid in the RCP conformation (Supplementary Fig. 1h–j). The results demonstrate that the FTIR difference signals between CAN<sub>RCP</sub> and CAN<sub>Dark</sub> would result in the 1550–75  $\text{cm}^{-1}$  bleach which clearly has a more pronounced shoulder in longer wavenumbers (violet dotted line, Supplementary Fig. 1j) as compared to the 1542  $\text{cm}^{-1}$  bleach characteristic of *s*-BP isomerization as shown on Fig. 1c. Our HFC predictions for the CAN<sub>RCP</sub> – CAN<sub>Dark</sub> difference IR spectrum thus agree very well with the EAS4 assignments.

## Discussion

Except for the final step of CTD/NTD separation, which is not achievable in crystals due to crystal packing constraints, amide-I FTIR kinetics data and assignments agree well with our crystallographic observations, indicating that the same photoinduced structural rearrangements occur both in OCP solutions and in crystals. This work provides the structural basis for the initial reaction in OCP light-activation. Our X-ray data demonstrates that the initial photoproduct involves the *s*-isomerization along C9'–C8' and C7'–C6' single bonds of CAN carotenoid in a BP manner. To propose how these reorientation motions could be driven by absorption of a photon, the carotenoid electronic structure needs to be considered. Light absorption in carotenoids like in other linear polyenes, is associated with  $S_0(1^1\text{Ag}^-) \rightarrow S_2(1^1\text{Bu}^+)$  transition, while the optically forbidden  $S_1$  dark state ( $2^1\text{Ag}^-$ ) is rapidly populated through internal conversion. Multiple reports indicate that the conical intersection driving the  $S_1(2^1\text{Ag}^-) \rightarrow S_0(1^1\text{Ag}^-)$  transition in polyenes of various length corresponds to a  $-(\text{CH}_3)-$  kink along the conjugated backbone, where several sequential bonds are totally or partially twisted<sup>45,46</sup>. We, therefore, put forward a hypothesis that the constrained protein environment of OCP drives the generation of the *s*-BP photoproduct as observed in II intermediate via CAN  $S_1$  state. For the *s*-BP photoproduct populated through  $S_1$  state to be cryotrapped after 1 min of illumination, the process should be extremely low in efficiency. Other possibility could be that isomerization of two double bonds followed by thermal reversion results in the *s*-BP photoproduct on such a time scale. However, the exact mechanism for the *s*-BP formation remains to be determined using methods allowing fs-ps time resolution (e.g., transient spectroscopy or serial crystallography).

UV/Vis and IR spectroscopic studies in combination with harmonic frequency calculations confirm the reaction mechanism in crystals and in solution. In response to the light-induced *s*-BP isomerization, structural changes propagate from the NTD to the CTD. The presented evidence shows that the H-bond rupture between the carotenoid and the CTD protein moiety does not initiate light activation but is a secondary event which follows post-isomerization NTD rearrangement.

While OCP has been shown to be active with different keto-carotenoids resulting in identical photocycle intermediates<sup>18,34</sup>, OCP with 3'-hECN was found to be the dominant form of OCP in native cyanobacteria<sup>13</sup>. Since the primary OCP photoproduct (CAN<sub>II</sub>) demonstrates two single bonds rotation around C9' and C6' carbons (Fig. 1c) in NTD during *s*-BP isomerization and does not involve the  $\beta_2$  ring, the mechanism observed here could also occur for OCP with different keto-carotenoids and, therefore, naturally occurring in cyanobacteria during photoprotection.

Previously, BP photoisomerization was observed in another conjugated chromophore, retinal<sup>26,27</sup>. However, in retinal the process involves aborted two-double-bond isomerization. The mechanism observed here involves two orchestrated single-bond isomerization steps in a BP manner and has not been reported before. Therefore, this finding is important for our understanding of carotenoid photophysics and evolution of photosensing of conjugated systems in general. Furthermore, the discovery of the overall OCP activation mechanism provides, for the first time, the foundation for gaining control and manipulation of the light regulation function of OCP with potential applications in optogenetics, bioimaging, and agriculture.

## Methods

### OCP expression

*E. coli* BL21-Gold (DE3) cells from Agilent Technologies were used for OCP expression. The OCP-encoding gene *slr1963* from *Synechocystis PCC 6803* was inserted between the NdeI/XhoI sites in the pET28 vector resulting in OCP-pET28 plasmid carrying G-S-S 6X His Tag-OCP at the NTD. To promote canthaxanthin (CAN) incorporation in vivo, the OCP-pET28 plasmid was co-expressed with pAC-CANTHipi plasmid (gift from Francis X Cunningham Jr, Addgene plasmid # 53301; <http://n2t.net/addgene:53301>; RRID:Addgene\_53301). The transformed cells were then grown in the presence of kanamycin (25  $\mu\text{M}/\text{ml}$ ) and chloramphenicol (25  $\mu\text{M}/\text{ml}$ ). Induction was carried out in LB medium at 37 °C for 3–4 h until the optical density at 600 nm ( $\text{OD}_{600}$ ) of 0.6–0.8 was reached. Then 0.2 mM IPTG was added to trigger OCP expression and the culture was grown for 16–18 h at 26 °C before harvesting the next day. After IPTG addition, *E. coli* cells were grown in the dark to prevent any OCP<sup>O</sup>–OCP<sup>R</sup> conversion. Cells were harvested and pelleted by centrifugation for 15 min at 5000  $\times g$  at 4 °C and were subsequently stored at –20 °C.

### OCP purification

Cell pellets were thawed and re-suspended in lysis buffer (40 mM Tris pH 8, 300 mM NaCl, and 10% glycerol) supplemented with DNase I (0.1 mg/ml) (Roche) and protease inhibitors (1 tablet per 100 ml) (Sigma) prior to cell disruption. All purification steps were carried out at 4 °C. Cell lysis was performed with two passes in a cell disrupter (Constant Systems Ltd.) at 40 kpsi. Broken cells then underwent ultra-centrifugation at 142,000  $\times g$  for 60 min before collecting the cell free extract and incubating it with pre-equilibrated HisTrap Ni<sup>2+</sup> resin (GE Healthcare) in a 3:1 volume ratio for 2 h under gentle shaking. Once the slurry was poured in a glass column, His-tagged OCP was washed with five column volumes (CV) of lysis buffer (wash 1) followed by three CV of lysis buffer supplement with 20 mM imidazole (wash 2). The protein was washed off with elution buffer (40 mM Tris pH 8, 300 mM NaCl, 10% glycerol, and 200 mM imidazole). Holo-OCP was subsequently separated from apo-OCP using anion exchange chromatography (DEAE 650 M) (Tosoh, Japan) by performing a 0–100 mM NaCl linear gradient. The concentration of Holo-OCP was determined using the maximum extinction coefficient of CAN (118,000  $\text{M}^{-1}\text{cm}^{-1}$ )<sup>47,48</sup> and the known 1:1 binding stoichiometry of CAN:OCP.

### Protein crystallization

OCP was washed with washing buffer (10 mM Tris pH 7.4) prior to crystallization using the sitting drop vapour diffusion method based on the protocol reported in<sup>10</sup> and described below: 2  $\mu\text{L}$  of OCP at 3 mg/mL was mixed with 1  $\mu\text{L}$  of reservoir solution (100 mM sodium acetate pH 4.5, 10% poly-ethylene glycol 20,000, 3% glycerol) and the drops were left to equilibrate at 20 °C for 5 days. Cubic crystals were flash frozen in liquid nitrogen after being transferred to a cryoprotectant solution consisting of the crystallization solution with 30% glycerol.

### Absorbance measurements- crystal pancakes

Slurries of OCP crystals were pelleted at  $1000 \times g$  and  $4^\circ\text{C}$  for 2 min and the supernatant removed. Pellets were scooped out and squeezed between two siliconized microscope coverslips using a micrometre to apply controlled force before sealing the edges with superglue. This process ensured the production of a pancake of crystalline matter with a reasonably uniform OD at 410 nm. The final OD<sub>410</sub> was typically around 0.2–0.3. Illumination was provided by a 10 W 410 nm Purple COB LED generating 100 mW of 410 nm light at the interaction area. The same LED with similar power was used for illumination of single crystals before flash freezing.

### Absorbance measurements- solutions

UV-VIS measurements were collected using an Agilent 8453 spectrophotometer. Samples with an OD<sub>500</sub> = 0.4 were used in a 1 cm light path quartz cuvette. Samples were kept at  $20^\circ\text{C}$  and illuminated with a 405 nm laser of 100 mW (Fig. 8a, b and Supplementary Fig. 1a) or variable power (Supplementary Fig. 1b, c) for 10 min (Fig. 8a, b) or for 40 s (Supplementary Fig. 1a). To confirm that the bicycle-pedal isomer relaxation is thermally-driven, the time-dependent UV-VIS spectra in Supplementary Fig. 1a were followed by 5 min of darkness after 40 s of illumination. Absorbance changes were collected at 0.5 s intervals.

### FTIR measurements

Fourier-transform infrared (FTIR) spectra were recorded at a  $1\text{ cm}^{-1}$  resolution using a Bio-Rad FTS 175 C FT-IR spectrophotometer equipped with a mercury cadmium telluride (MCT) detector. Before measurements the instrument was purged with CO<sub>2</sub>-free dry air for 120 min. Absorption spectra were collected in the region between 1700 and  $1500\text{ cm}^{-1}$ . For FTIR measurements, OCP in its original buffer (40 mM Tris pH 8, 10% glycerol) was exchanged into either H<sub>2</sub>O (40 mM Tris pH 8) or D<sub>2</sub>O (40 mM Tris pD 8) based buffers. 10  $\mu\text{L}$  of sample previously concentrated to the maximum achievable concentration was placed into the Harrick cell fitted with a 6  $\mu\text{m}$  spacer to obtain an OD<sub>500</sub> around 0.2. First, FTIR was measured in a dark-adapted (non-illuminated) state consisting of 2000 interferograms. The sample was then illuminated at 405 nm with a 100 mW laser. Each FTIR spectrum containing 100 interferograms was recorded in 35 s. A total of 16 spectra were collected sequentially for about 10 min after the onset of illumination.

### Global fit of spectroscopic data

The obtained absorbance changes were analyzed globally using Glotaran software<sup>35</sup> and the methodology described in<sup>36</sup>. During the global analysis UV-VIS and FTIR datasets (both D<sub>2</sub>O and H<sub>2</sub>O) were linked together. The unbranched and unidirectional, so-called sequential model (EAS1→EAS2→...→EAS<sub>n,comp</sub>) was used, where EAS stands for Evolution Associated Spectra. During the global analysis, UV-VIS and FTIR datasets in both D<sub>2</sub>O and H<sub>2</sub>O buffers were linked together.

### Sample optimization and X-ray crystallography

OCP crystals had cubic morphology. The cubes with the length of not more than 30  $\mu\text{m}$  were selected for the illumination experiment to allow light penetration through the crystal. Taking into account unit cell dimensions and CAN extinction coefficient ( $118,000\text{ M}^{-1}\text{ cm}^{-1}$ )<sup>47,48</sup> OD of single crystals is  $\sim 1.0$ . Therefore only a few percent of absorbed light are transmitted. As a result, overall populations of illuminated states do not exceed 30% in single crystals. Illumination was performed at RT using a 10 W 410 nm Purple COB LED generating 100 mW of 410 nm light at the interaction area. Great care was taken so that the crystal was evenly exposed to the set illuminated intensity over the desired illumination time. After preillumination the crystals were flash frozen in liquid nitrogen after being gradually transferred to a cryoprotectant solution (crystallization solution with 30% glycerol). To be sure that no build-up intermediates would relax the crystals were also

illuminated while moving into cryoprotectant or in liquid N<sub>2</sub>. The crystals were illuminated for different final time illuminated periods: 1 min (I1), 2 min (I2), 5 min (I3), and 10 min (I4). After the illuminated crystals have been cryotrapped they were sent to Diamond Light source for data collection. All X-ray diffraction data collection was carried out at i03 and i04 beamlines (Diamond Light Source, UK).

### X-ray data refinement

OCP crystals belonged to the P<sub>3</sub>21 space group with  $a = 82.5\text{ \AA}$ ,  $b = 82.5\text{ \AA}$ , and  $c = 87.3\text{ \AA}$ . Diffraction data were integrated through xia2 pipeline with DIALS<sup>49</sup>. The structures were solved by molecular replacement with MOLREP<sup>50</sup> using a starting model based on the PDB ID 4XB5. Refinement was performed with REFMAC<sup>51</sup> alternating with/ model building using 2Fo-Fc and Fo-Fc maps visualized in COOT<sup>52</sup>. The final model contains one OCP molecule in the asymmetric unit. Statistics for diffraction data collection, structure determination and refinement are summarized in Supplementary Table 1.

DED maps, calculated for various dark datasets ( $F_{\text{Dark}} - F_{\text{Dark}}$ ) reveal no map features, indicating that the different “dark” structures are identical and do not exhibit any spatial arrangement differences as expected (Fig. 3a). DED maps were generated using Q-weighted method (see Extrapolated maps and coordinates). In all four cases, the obtained difference maps in different states are highly reproducible (Fig. 3). The results indicate that the signals must be generated by actual biological phenomenon during OCP light-activation and do not arise from statistical noise. Similar difference signals were also obtained using phenix.fobs\_minus\_fobs\_map method. Figures of crystal structures and difference maps were visualized using PyMOL Molecular Graphics System (Version 2.5.0, [www.pymol.org](http://www.pymol.org)).

Difference density amplitudes were obtained according to<sup>53</sup>. In short, difference amplitudes  $A_i(a_i)$  and difference Fourier electron density maps within spheres of radius  $2.0\text{ \AA}$  centred upon atom  $a_i$  were averaged using a  $3\sigma$  cut-off and a  $0.5\text{ \AA}$  grid spacing.

### Extrapolated maps and coordinates

To generate extrapolated maps firstly, DED were calculated using the Fourier transform of weighted difference structure amplitudes based on the Bayesian statistics analysis by Ursby et al.<sup>30,54</sup>. For each corresponding structure factor difference ( $\Delta F$ ) between the light ( $F_L$ ) and dark ( $F_D$ ) data, a weighted factor ( $w$ ) was calculated and applied to the difference as implemented in<sup>55–57</sup>. Light, dark and calculated structure factors were combined using CAD and scaled using the anisomorphous option in Scale<sup>54</sup>. This placed each set of structure factors onto a normalized absolute scale compared to the calculated structure factors ( $F_C$  calculated using SFALL). The final real-space map was calculated using FFT. Phases from the dark state structure, corresponding to unilluminated OCP crystals were used<sup>54</sup>. To identify small structural changes in the illuminated data, extrapolated electron density maps were generated and extrapolated coordinates then refined to these maps. Difference structure factors were added in a linear combination in multiples of  $N_{\text{EXT}}$  to the calculated dark structure ( $F_{\text{Dark}}$ ) in order to generate extrapolated structure factors ( $F_{\text{EXT}}$ ). The negative electron density around areas of interest in the protein were then integrated. The point where negative density started to build-up was used to determine a characteristic  $N_{\text{EXT}}$  value which was then used to generate the final extrapolated structure factors. The population transfer (PT) was around 15–30% as can be approximated from the  $N_{\text{EXT}}$  value ( $\text{PT} = 200/N_{\text{EXT}}$ )<sup>57</sup>. Coordinates were refined against the extrapolated structure factors using five cycles of rigid body refinement in REFMAC<sup>58</sup>. The real space refinement tool on COOT<sup>52</sup> was used to fit the carotenoid and neighbouring amino acids to the extrapolated electron density. These coordinates were then saved and used for the occupancy refinement against the ground state/dark structure for I1–I4 datasets. Occupancy refers to the proportion of extrapolated coordinates (light, I1–I4) compared to ground state coordinates



(OCP<sup>0</sup>). Both  $R$  and  $R_{\text{free}}$  minimize at the occupancies: Dark = 0.84/Light = 0.16 (I1), Dark = 0.78/Light = 0.22 (I1), Dark = 0.75/Light = 0.25 (I1) and Dark = 0.68/Light = 0.32 (I4).

### Long-wavelength experiment

The crystals were harvested using LithoLoop (Molecular Dimensions) sample mounts on specialized I23 copper sample assemblies. Data were collected on the long-wavelength beamline I23<sup>59</sup> at Diamond Light Source with X-ray energies of 2.9 keV ( $\lambda = 4.28\text{\AA}$ ) and 2.8 keV ( $\lambda = 4.43\text{\AA}$ ) using a semi-cylindrical PILATUS 12 M detector (Dectris, CH). These energies were selected as they are above and below the Cl absorption edge ( $E = 2.82\text{ keV}/\lambda = 4.39\text{\AA}$ ) respectively, thus allowing for Cl identification during analysis of anomalous difference Fourier maps. Sweeps of 360° with an exposure time of 0.1 s per 0.1° image were taken using the same crystal. To ensure completeness, two datasets for each energy were collected with the multi-axis goniometer at angles  $\kappa = 0^\circ$  and  $\varphi = 0^\circ$  and, subsequently,  $\kappa = -30^\circ$  and  $\varphi = 60^\circ$ . These datasets were interleaved to mitigate radiation damage effects.

For data processing, data integration was performed with XDS and XSCALE programmes. The origin of the PDB model was corrected using POINTLESS, AIMLESS and MOLREP. Phased anomalous difference Fourier maps were produced using ANODE. A cut-off of 6.0  $\sigma$  was used to identify sites of anomalous contribution.

### Harmonic frequency calculations

The Gaussian 06 software package<sup>60,61</sup> and the Becke-3-Lee-Yang-Parr functional<sup>62</sup> were used with the 6-311+G basis set. Theoretical IR values for frequencies and intensities in CAN were calculated for the three states CAN<sub>Dark</sub> (Fig. 8d), CAN<sub>I1</sub> (Fig. 8d), CAN<sub>I4</sub> (Supplementary Fig. 1i), and for the RCP structure as reported in ref. 10 (Supplementary Fig. 1j). FTIR spectra were derived from the theoretical IR values using Gaussian programme by assigning FWHM with spreading the intensity over a Lorentzian function. The Lorentzian line width for each absorption peak in the calculation was taken to be 4 cm<sup>-1</sup>. The optimization of molecular geometry was performed with fixing all CAN dihedral angles. As a control, FTIR spectra were also calculated for CAN<sub>I1</sub> and CAN<sub>Dark</sub> optimized geometries where dihedral angles were not fixed (Supplementary Fig. 1h). The CAN<sub>I1</sub> – CAN<sub>Dark</sub> difference signal in Supplementary Fig. 1h results in a similar bleach observed in Fig. 8d but with lower amplitude and a shift to lower wavenumbers.

A scaling factor of 0.97<sup>63–65</sup> was used to convert the calculated theoretical frequencies to FTIR spectra.

### Reporting summary

Further information on research design is available in the Nature Research Reporting Summary linked to this article.

### Data availability

Coordinates and structure factors have been deposited in the Protein Data Bank under the following accession codes: 7ZSF (OCP<sup>0</sup>), 7ZSG (I1), 7ZSH (I2), 7ZSI (I3) and 7ZSJ (I4).

Furthermore, the crystal structures of OCP used in this study are available in the Protein Data Bank under the following accession codes: 4XB5, 5TUX 5UI2. Source data are provided as a Source Data file. Source data are provided with this paper.

### References

- Maoka, T. Carotenoids as natural functional pigments. *J. Nat. Med.* **74**, 1–16 (2020).
- Polivka, T. & Sundstrom, V. Ultrafast dynamics of carotenoid excited States-from solution to natural and artificial systems. *Chem. Rev.* **104**, 2021–2071 (2004).
- Polivka, T. & Frank, H. A. Molecular factors controlling photo-synthetic light harvesting by carotenoids. *Acc. Chem. Res.* **43**, 1125–1134 (2010).
- Ruban, A. V. et al. Identification of a mechanism of photoprotective energy dissipation in higher plants. *Nature* **450**, 575–578 (2007).
- Kromdijk, J. et al. Improving photosynthesis and crop productivity by accelerating recovery from photoprotection. *Science* **354**, 857–861 (2016).
- Liguori, N. et al. Different carotenoid conformations have distinct functions in light-harvesting regulation in plants. *Nat. Commun.* **8**, 1–9 (2017).
- Pascal, A. A. et al. Molecular basis of photoprotection and control of photosynthetic light-harvesting. *Nature* **436**, 134–137 (2005).
- Muzzopappa, F. & Kirilovsky, D. Changing color for photoprotection: The Orange Carotenoid Protein. *Trends Plant Sci.* **25**, 92–104 (2020).
- Kerfeld, C. A. et al. The crystal structure of a cyanobacterial water-soluble carotenoid binding protein. *Structure* **11**, 55–65 (2003).
- Leverenz, R. L. et al. A 12 Å carotenoid translocation in a photo-switch associated with cyanobacterial photoprotection. *Science* **348**, 1463–1466 (2015).
- Gupta, S. et al. Local and global structural drivers for the photo-activation of the orange carotenoid protein. *Proc. Natl Acad. Sci. USA* **112**, E5567–E5574 (2015).
- Gwizdala, M., Wilson, A. & Kirilovsky, D. In vitro reconstitution of the cyanobacterial photoprotective mechanism mediated by the Orange Carotenoid Protein in *Synechocystis* PCC 6803. *Plant Cell* **23**, 2631–2643 (2011).
- Wilson, A. et al. A photoactive carotenoid protein acting as light intensity sensor. *Proc. Natl Acad. Sci. USA* **105**, 12075–12080 (2008).
- Kirilovsky, D. & Kerfeld, C. A. The Orange Carotenoid Protein: A blue-green light photoactive protein. *Photochem. Photobiol. Sci.* **2**, 1135–1143 (2013).
- Wilson, A. et al. Structural determinants underlying photoprotection in the photoactive orange carotenoid protein of cyanobacteria. *J. Biol. Chem.* **285**, 18364–18375 (2010).
- Wilson, A. et al. The essential role of the N-terminal domain of the orange carotenoid protein in cyanobacterial photoprotection: Importance of a positive charge for phycobilisome binding. *Plant Cell* **24**, 1972–1983 (2012).
- Bandara, S. et al. Photoactivation mechanism of a carotenoid-based photoreceptor. *Proc. Natl Acad. Sci. USA* **114**, 6286–6291 (2017).
- Konold, P. E. et al. Photoactivation mechanism, timing of protein secondary structure dynamics and carotenoid translocation in the Orange Carotenoid Protein. *J. Am. Chem. Soc.* **141**, 520–530 (2019).
- Bondanza, M., Cupellini, L., Lipparini, F. & Mennucci, B. The multiple roles of the protein in the photoactivation of Orange Carotenoid Protein. *Chem* **6**, 187–203 (2020).
- Wilson, A., Punginelli, C., Couturier, M., Perreau, F. & Kirilovsky, D. Essential role of two tyrosines and two tryptophans on the photoprotection activity of the Orange Carotenoid Protein. *Biochim. Biophys. Acta-Bioenerg.* **1807**, 293–301 (2011).
- Yaroshevich, I. A. et al. Role of hydrogen bond alternation and charge transfer states in photoactivation of the Orange Carotenoid Protein. *Commun. Biol.* **4**, 1–13 (2021).
- Wei, T., Balevicius, V., Polivka, T., Ruban, A. V. & Duffy, C. D. P. How carotenoid distortions may determine optical properties: Lessons from the orange carotenoid protein. *Phys. Chem. Chem. Phys.* **21**, 23187–23197 (2019).
- Nogly, P. et al. Retinal isomerization in bacteriorhodopsin captured by a femtosecond X-ray laser. *Science* **361**, eaat0094 (2018).
- Gurchiek, J. K. et al. Fluorescence and excited-state conformational dynamics of the Orange Carotenoid Protein. *J. Phys. Chem. B* **122**, 1792–1800 (2018).
- von Lintig, J. & Vogt, K. Filling the gap in vitamin A research: Molecular identification of an enzyme cleaving  $\beta$ -carotene to retinal. *J. Biol. Chem.* **275**, 11915–11920 (2000).

26. Warshel, A. Bicycle-pedal model for the first step in the vision process. *Nature* **260**, 679–683 (1976).
27. Frutos, L. M., Andruniów, T., Santoro, F., Ferré, N. & Olivucci, M. Tracking the excited-state time evolution of the visual pigment with multiconfigurational quantum chemistry. *Proc. Natl. Acad. Sci. USA* **104**, 7764–7766 (2007).
28. Altoè, P., Cembran, A., Olivucci, M. & Garavelli, M. Aborted double bicycle-pedal isomerization with hydrogen bond breaking is the primary event of bacteriorhodopsin proton pumping. *Proc. Natl. Acad. Sci. USA* **107**, 20172–20177 (2010).
29. Nass Kovacs, G. et al. Three-dimensional view of ultrafast dynamics in photoexcited bacteriorhodopsin. *Nat. Commun.* **10**, 1–17 (2019).
30. Ursby, T. & Bourgeois, D. Improved estimation of structure-factor difference amplitudes from poorly accurate data. *Acta Crystallogr. Sect. A Found. Crystallogr.* **53**, 564–575 (1997).
31. Pande, K. et al. Femtosecond structural dynamics drives the trans/cis isomerization in photoactive yellow protein. *Science* **352**, 725–729 (2016).
32. Schapiro, I., Weingart, O. & Buss, V. Bicycle-pedal isomerization in a rhodopsin chromophore model. *J. Am. Chem. Soc.* **131**, 16–17 (2009).
33. Saltiel, J., Krishna, T. S. R., Laohasurayotin, S., Fort, K. & Clark, R. J. Photoisomerization of cis, cis-to trans, trans-1, 4-Diaryl-1, 3-butadienes in the solid state: The bicycle-pedal mechanism. *J. Phys. Chem. A* **112**, 199–209 (2008).
34. Mezzetti, A. et al. Two-step structural changes in Orange Carotenoid Protein photoactivation revealed by time-resolved Fourier transform infrared spectroscopy. *J. Phys. Chem. B* **123**, 3259–3266 (2019).
35. Snellenburg, J. J., Liptonok, S. P., Seger, R., Mullen, K. M. & van Stokkum, I. H. M. Glotaran: A Java-based graphical user interface for the R Package TIMP. *J. Stat. Softw.* **49**, 1–22 (2012).
36. van Stokkum, I. H. M., Larsen, D. S. & van Grondelle, R. Global and target analysis of time-resolved spectra. *Biochim. Biophys. Acta-Bioenerg.* **1657**, 82–104 (2004).
37. Holzwarth, A. *Biophysical Techniques in Photosynthesis* (eds. Amesz, J. & Hoff, A.) Vol. **3**, 75–92 (Springer Netherlands, 1996).
38. Zechmeister, L. & Polgár, A. Cis-trans isomerization and spectral characteristics of carotenoids and some related compounds. *J. Am. Chem. Soc.* **65**, 1522–1528 (1943).
39. Polgár, A. & Zechmeister, L. Action of cold concentrated hydriodic acid on carotenes: Structure and cis-trans-isomerization of some reaction products. *J. Am. Chem. Soc.* **65**, 1528–1534 (1943).
40. Philip, T. & Francis, F. J. Isolation and chemical properties of capsanthin and derivatives. *J. Food Sci.* **36**, 823–827 (1971).
41. Schlücker, S., Szeghalmi, A., Schmitt, M., Popp, J. & Kiefer, W. Density functional and vibrational spectroscopic analysis of  $\beta$ -carotene. *J. Raman Spectrosc.* **34**, 413–419 (2003).
42. Berezin, K. V. & Nechaev, V. V. Calculation of the IR spectrum and the molecular structure of  $\beta$ -carotene. *J. Appl. Spectrosc.* **72**, 164–171 (2005).
43. Punginelli, C., Wilson, A., Routaboul, J. M. & Kirilovsky, D. Influence of zeaxanthin and echinenone binding on the activity of the orange carotenoid protein. *Biochim. Biophys. Acta-Bioenerg.* **1787**, 280–288 (2009).
44. Akhtar, M. & Weedon, B. C. L. 814. Carotenoids and related compounds. Part VIII. Novel syntheses of echinenone and canthaxanthin. *J. Chem. Soc.* **814**, 4058–4062 (1959).
45. Celani, P. et al. Molecular “trigger” for the radiationless deactivation of photoexcited conjugated hydrocarbons. *J. Am. Chem. Soc.* **117**, 11584–11585 (1995).
46. Garavelli, M. et al. Relaxation paths and dynamics of photoexcited polyene chains: Evidence for creation and annihilation of neutral soliton pairs. *J. Am. Chem. Soc.* **122**, 5568–5581 (2000).
47. Britton, G., Liaaen-Jensen, S. & Pfander, H. (ed.). *Carotenoids: Handbook* (Springer Science & Business Media, 2004).
48. Jeffrey, S. W. *Phytoplankton Pigments in Oceanography: Guidelines to Modern Methods* (Unesco Pub., 2005). Appendix: Chlorophyll and carotenoid extinction coefficients.
49. Waterman, D. G. et al. The DIALS framework for integration software. *CCP4 Newsl. Protein Crystallogr.* **49**, 13–15 (2013).
50. Vagin, A. & Teplyakov, A. MOLREP: An automated program for molecular replacement. *J. Appl. Crystallogr.* **30**, 1022–1025 (1997).
51. Vagin, A. A. et al. REFMAC5 dictionary: Organization of prior chemical knowledge and guidelines for its use. *Acta Crystallogr. Sect. D. Biol. Crystallogr.* **60**, 2184–2195 (2004).
52. Emsley, P. & Cowtan, K. Coot: Model-building tools for molecular graphics. *Acta Crystallogr. Sect. D. Biol. Crystallogr.* **60**, 2126–2132 (2004).
53. Wickstrand, C. et al. A tool for visualizing protein motions in time-resolved crystallography. *Struct. Dyn.* **7**, 024701 (2020).
54. Winn, M. D. et al. Overview of the CCP4 suite and current developments. *Acta Crystallogr. Sect. D. Biol. Crystallogr.* **67**, 235–242 (2011).
55. Schmidt, M., Rajagopal, S., Ren, Z. & Moffat, K. Application of singular value decomposition to the analysis of time-resolved macromolecular X-ray data. *Biophys. J.* **84**, 2112–2129 (2003).
56. Ren, Z. et al. A molecular movie at 1.8 Å resolution displays the photocycle of photoactive yellow protein, a eubacterial blue-light receptor, from nanoseconds to seconds. *Biochemistry* **40**, 13788–13801 (2001).
57. Pandey, S. et al. Time-resolved serial femtosecond crystallography at the European XFEL. *Nat. Methods* **17**, 73–78 (2020).
58. Murshudov, G. N. et al. REFMAC5 for the refinement of macromolecular crystal structures. *Acta Crystallogr. Sect. D. Biol. Crystallogr.* **67**, 355–367 (2011).
59. Wagner, A., Duman, R., Henderson, K. & Mykhaylyk, V. In-vacuum long-wavelength macromolecular crystallography. *Acta Crystallogr. Sect. D. Struct. Biol.* **72**, 430–439 (2016).
60. Frisch, M. J. et al. *Gaussian 09, Revision B.01* (Gaussian, Inc., Wallingford CT, 2009).
61. Becke, A. D. Density-functional thermochemistry. III. The role of exact exchange. *J. Chem. Phys.* **98**, 5648 (1993).
62. Lee, C., Yang, W. & Parr, R. G. Development of the Colle-Salvetti correlation-energy formula into a functional of the electron density. *Phys. Rev. B* **37**, 785 (1988).
63. Macernis, M., Sulskus, J., Malickaja, S., Robert, B. & Valkunas, L. Resonance Raman spectra and electronic transitions in carotenoids: A density functional theory study. *J. Phys. Chem. A* **118**, 1817–1825 (2014).
64. Wong, M. W. Vibrational frequency prediction using density functional theory. *Chem. Phys. Lett.* **256**, 391–399 (1996).
65. Mezzetti, A., Kish, E., Robert, B. & Spezia, R. Assignment of IR bands of isolated and protein-bound Peridinin in its fundamental and triplet state by static FTIR, time-resolved step-scan FTIR and DFT calculations. *J. Mol. Struct.* **1090**, 58–64 (2015).

## Acknowledgements

The data were collected remotely at Diamond Light Source (BAG proposal number mx17221). This project was supported by the EMBO long-term fellowship (EMBO ALTF 244-2017) and has received funding from the European Union Horizon 2020 research and innovation programme under the Marie Skłodowska-Curie grant (agreement No. 839389) to V.C. This work was supported by the Leverhulme Trust award RPG-2018-372. The crystallization facility at Imperial College was funded by the BBSRC (BB/D524840/1) and Wellcome Trust (202926/Z/16/Z). We thank Violeta Cordon Preciado for technical assistance.

## Author contributions

V.U.C. designed the project. V.U.C. expressed and purified OCP protein, prepared OCP crystals, collected and processed X-ray data and UV-VIS/FTIR data. J.M.B. assisted with creating Q-weighted maps and extrapolated coordinates. A.F. and J.J.v.T. performed Harmonic Oscillator Calculations. R.M.M. assisted with cryo trapping experiment and X-ray data processing. M.A.P. assisted with the designing of OCP expression system in *E.coli*, while K.M. provided advice and support in obtaining OCP crystals. C.O. and A.W. performed long wavelength experiments. V.U.C. wrote the manuscript with the input from J.B., R.M.M., A.F., C.O. and A.W. J.M.B., R.M.M., A.F., C.O., A.W. and in particular K.M., V.U.C., and J.J.v.T. contributed to the review and editing. J.J.v.T. supervised the project.

## Competing interests

The authors declare no competing interests.

## Additional information

**Supplementary information** The online version contains supplementary material available at <https://doi.org/10.1038/s41467-022-34137-4>.

**Correspondence** and requests for materials should be addressed to Jasper J.van Thor.

**Peer review information** *Nature Communications* thanks Jan Kern, Massimo Olivucci and the other, anonymous, reviewer(s) for their contribution to the peer review of this work.

**Reprints and permissions information** is available at <http://www.nature.com/reprints>

**Publisher's note** Springer Nature remains neutral with regard to jurisdictional claims in published maps and institutional affiliations.

**Open Access** This article is licensed under a Creative Commons Attribution 4.0 International License, which permits use, sharing, adaptation, distribution and reproduction in any medium or format, as long as you give appropriate credit to the original author(s) and the source, provide a link to the Creative Commons license, and indicate if changes were made. The images or other third party material in this article are included in the article's Creative Commons license, unless indicated otherwise in a credit line to the material. If material is not included in the article's Creative Commons license and your intended use is not permitted by statutory regulation or exceeds the permitted use, you will need to obtain permission directly from the copyright holder. To view a copy of this license, visit <http://creativecommons.org/licenses/by/4.0/>.

© The Author(s) 2022